



HAL
open science

North-South Asymmetric Kelvin-Helmholtz Instability and Induced Reconnection at the Earth's Magnetospheric Flanks

S. Fadanelli, Matteo Faganello, F. Califano, S. S Cerri, F. Pegoraro, B.
Lavraud

► **To cite this version:**

S. Fadanelli, Matteo Faganello, F. Califano, S. S Cerri, F. Pegoraro, et al.. North-South Asymmetric Kelvin-Helmholtz Instability and Induced Reconnection at the Earth's Magnetospheric Flanks. *Journal of Geophysical Research Space Physics*, 2018, 123 (11), pp.9340-9356. 10.1029/2018JA025626 . hal-03101806

HAL Id: hal-03101806

<https://hal.science/hal-03101806>

Submitted on 7 Jan 2021

HAL is a multi-disciplinary open access archive for the deposit and dissemination of scientific research documents, whether they are published or not. The documents may come from teaching and research institutions in France or abroad, or from public or private research centers.

L'archive ouverte pluridisciplinaire **HAL**, est destinée au dépôt et à la diffusion de documents scientifiques de niveau recherche, publiés ou non, émanant des établissements d'enseignement et de recherche français ou étrangers, des laboratoires publics ou privés.

1 **North-South asymmetric Kelvin-Helmholtz instability and**
2 **induced reconnection at the Earth's magnetospheric flanks**

3 S. Fadanelli^{1,2} M. Faganello³ F. Califano¹ S. S. Cerri⁴ F. Pegoraro¹ B. Lavraud²

4 ¹Dipartimento di Fisica "E. Fermi", Università di Pisa, Largo B. Pontecorvo 3, 56127 Pisa, Italy

5 ²IRAP, Université de Toulouse, CNRS, CNES, UPS, (Toulouse), France

6 ³Aix-Marseille University, CNRS, PIIM UMR 7345, 13397, Marseille, France

7 ⁴Department of Astrophysical Sciences, Princeton University, 4 Ivy Ln, Princeton, NJ 08544, USA

8 **Abstract**

9 We present a three-dimensional study of the plasma dynamics at the flank magnetopause of
10 the Earth's magnetosphere during mainly northward interplanetary magnetic field (IMF) pe-
11 riods. Two-fluid simulations show that the initial magnetic shear at the magnetopause and
12 the field line bending caused by the dynamics itself (in a configuration taken as represen-
13 tative of the properties of the flank magnetopause) influence both the location where the
14 Kelvin-Helmholtz (KH) instability and the induced magnetic reconnection take place and
15 their nonlinear development. The KH vortices develop asymmetrically with respect to the
16 Earth's equatorial plane where the local KH linear growth rate is maximal. Vortex driven re-
17 connection processes take place at different latitudes, ranging from the equatorial plane to
18 mid-latitude regions, but only in the hemisphere that turns out to be the less KH unstable.
19 These results suggest that KH-induced reconnection is not limited to specific regions around
20 the vortices (inside, below or above), but may be triggered over a broad and continuous range
21 of locations in the vicinity of the vortices.

22 **1 Introduction**

23 The large-scale dynamics of the Earth's magnetosphere can be modelled, as a first ap-
24 proach, adopting a one-fluid magnetohydrodynamic (MHD) description. In fact the magne-
25 toospheric plasma follows an "ideal" dynamics over most of its spatial domain, the magnetic
26 field lines being frozen into the plasma motion and any cross-field diffusion being fairly neg-
27 ligible [Sonnerup, 1980; Labelle and Treumann, 1988; Le et al., 1994]. The magnetospheric
28 region where field lines are "anchored" to the Earth is separated from the heated solar wind
29 plasma of the magnetosheath, where the interplanetary magnetic field (IMF) lines are con-
30 nected to the open space, by a magnetic boundary known as the magnetopause.

31 Independently of its complex magnetic shape, in the absence of cross-field diffusion
32 the frozen-in law prevents any kind of mixing between the magnetospheric and the solar
33 wind plasmas. Therefore the plasma of solar wind origin could not in principle enter into
34 the less dense magnetosphere.

35 However, the frozen-in condition can be locally violated by non-ideal effects arising at
36 small scales generated by the plasma dynamics itself, e.g. allowing for magnetic reconnec-
37 tion to occur. Since reconnection is capable of modifying the global magnetic field topology,
38 it strongly impacts both the dynamics of the whole system and the transport properties at the

39 magnetopause. In particular during southward periods when the IMF direction is opposite
40 to that of the magnetospheric magnetic field at low latitude, reconnection occurs at dayside
41 magnetopause allowing for direct transport across the magnetopause and leading to the for-
42 mation of a low-latitude boundary layer (LLBL) where solar wind and magnetospheric plas-
43 mas can mix [Dungey, 1961].

44 During northward periods the magnetic configuration at the low latitude magnetopause
45 is unfavourable for magnetic reconnection to occur. Nevertheless the formation of a LLBL is
46 observed also during these periods [Mitchell *et al.*, 1987] up to the point that the entry of so-
47 lar wind particles into the magnetosphere can be even more important than during southward
48 periods [Terasawa *et al.*, 1997]. Different mechanisms have been invoked for explaining this
49 transport which is routinely observed by satellites.

50 The non linear vortex dynamics resulting from the development of the Kelvin-Helmholtz
51 (KH) instability is one of the few phenomena, together with lobe reconnection [Gosling
52 *et al.*, 1991; Song and Russell, 1992; Onsager *et al.*, 2001] and kinetic Alfvén waves [John-
53 son *et al.*, 2001; Johnson and Cheng, 2001; Chaston *et al.*, 2007], able to explain the ob-
54 served transport (see, e.g., Faganello and Califano [2017] for further details on the respective
55 role of the different phenomena). The KH instability is driven by the velocity shear between
56 the stagnant magnetosphere and the flowing magnetosheath plasma of solar wind origin and
57 grows along the magnetospheric flanks at low latitude, where the stabilizing magnetic shear
58 is weaker for northward IMF. By contrast, under such northward IMF conditions, higher lati-
59 tude regions are instead completely stabilized by the stronger magnetic shear.

60 *Per se*, the KH vortices developing during the non-linear phase can strongly perturb the
61 magnetopause but cannot mix the two different plasmas as their typical scale is so large that
62 their early dynamics remains “MHD-ideal”. However, they become the driver of very fast
63 secondary instabilities which give rise to a rich, small-scale non-linear dynamics that feeds
64 on the energy source provided by the vortical motion: from secondary Kelvin-Helmholtz
65 and Rayleigh-Taylor instabilities [Matsumoto and Hoshino, 2004; Faganello *et al.*, 2008a;
66 Tenerani *et al.*, 2011; Nakamura and Daughton, 2014], to magnetic reconnection [Knoll and
67 Brackbill, 2002; Nakamura *et al.*, 2006; Otto and Fairfield, 2000; Faganello *et al.*, 2008b,
68 2012a], magnetorotational instability [Matsumoto and Seki, 2007] or current-sheet kink in-
69 stability [Nakamura *et al.*, 2004].

70 If a magnetic shear exists across the low-latitude magnetopause, the KH velocity field
71 will eventually pinch the magnetopause current sheet in between vortices and force the so-
72 called “Type I” vortex induced reconnection to occur there [*Liu and Hu*, 1988]. In this case
73 reconnection must proceed on nearly the same ideal time-scale of the vortex dynamics in
74 order to release the magnetic energy that piles-up at the compressed current sheet carried
75 by the ideal motion [*Chen et al.*, 1997; *Knoll and Brackbill*, 2002; *Nakamura et al.*, 2006,
76 2013]. Type I reconnection creates field lines that thread through the magnetopause, leading
77 to a direct entry of solar wind particle into the magnetosphere.

78 If the initial magnetic shear is set to zero and high-latitude KH stable region are in-
79 cluded in the model, it has been shown that reconnection develops first at mid-latitude in-
80 stead of around the equatorial plane where the vortices are generated by the primary KH in-
81 stability. This process is driven by the braiding and the stretching of the field lines advected
82 by the vortices at the equator but remaining anchored at higher latitudes in the Earth’s mag-
83 netosphere [*Faganello et al.*, 2012a, 2014].

84 Under such conditions, mid-latitude reconnection develops almost symmetrically with
85 respect to the equatorial plane and creates double-reconnected flux tubes. These newly closed
86 flux tubes, located on the Earthward side of the magnetopause, thus become populated with
87 dense solar wind plasma. In this way, solar wind plasma enters the magnetosphere at a rate
88 that is compatible with the observed one [*Faganello et al.*, 2012a].

89 Recently, MMS spacecraft data have provided unambiguous in situ evidence of mag-
90 netic reconnection which were interpreted as Type I reconnection at the compressed current
91 sheets forming in between primary successive KH vortices [*Eriksson et al.*, 2016], confirm-
92 ing past observations with Cluster [*Nykyri et al.*, 2006; *Hasegawa et al.*, 2009]. Remarkably,
93 for the same MMS event evidences were also found for remote reconnection [*Vernisse et al.*,
94 2016], i.e. occurring far away from the satellite location, as signalled by heated ions and
95 electrons flowing parallel and anti-parallel along magnetic field lines just outside the mag-
96 netopause (e.g. *Gosling et al.* [1991]; *Fuselier et al.* [1995]; *Lavraud et al.* [2006]). These
97 results suggest that Type I and mid-latitude reconnection coexist and cooperate in forming
98 the LLBL for northward IMF, when a magnetic shear is present.

99 Here we present a numerical study that takes into account both a pre-existing shear be-
100 tween the magnetospheric field and the IMF, as well as the high-latitude stabilization of the
101 KH instability, allowing for the simultaneous development of Type I and mid-latitude recon-

102 nection. In Sec. 2 we present the plasma model, the initial equilibrium and the parameters
 103 used in our simulations. In Sec. 3 we show how the large-scale structures of the vortices are
 104 modified when both magnetic shear and high-latitude stabilization are present. In Sec. 4 we
 105 present the analysis of the KH-induced reconnection processes. Finally, in Sec. 5 conclu-
 106 sions are drawn.

107 **2 Plasma model and simulation setup**

108 We adopt a Hall-MHD plasma model (including finite resistivity). The model equa-
 109 tions, in conservative form, are:

$$110 \quad \partial_t n + \nabla \cdot (n\mathbf{u}) = 0 \quad (1)$$

$$111 \quad \partial_t (n\mathbf{u}) + \nabla \cdot (n\mathbf{u}\mathbf{u} + P_{tot}\bar{\mathbf{I}} - \mathbf{B}\mathbf{B}) = \mathbf{0} \quad (2)$$

$$112 \quad \partial_t \mathbf{B} = -\nabla \times \mathbf{E} \quad (3)$$

$$\mathbf{E} = -\mathbf{u} \times \mathbf{B} + \mathbf{J}/n \times \mathbf{B} - \nabla P_e / n + \eta \mathbf{J} \quad (4)$$

113 where all quantities are normalized to ion (proton) quantities, the ion mass m_i , the inertial
 114 length d_i and the Alfvén speed v_A . Here n is the plasma number density, $\mathbf{u} \simeq \mathbf{u}_i$ the fluid
 115 velocity and $P_{tot} = P_i + P_e + B^2/2$. The ion and electron thermal pressures are evolved
 116 following an ideal adiabatic closure:

$$117 \quad \partial_t (nS_{i,e}) + \nabla \cdot (nS_{i,e}\mathbf{u}_{i,e}) = 0 \quad ; \quad S_{i,e} = P_{i,e}n^{-5/3} \quad (5)$$

118 Finally, we neglect the displacement current; then, the Faraday equation and the electron
 119 fluid velocity are given by

$$120 \quad \mathbf{J} = \nabla \times \mathbf{B} \quad ; \quad \mathbf{u}_e = \mathbf{u} - \mathbf{J}/n \quad (6)$$

121
 122
 123 With this model, during the initial large-scale dynamics leading to the formation of
 124 fully rolled-up KH vortices, the magnetic field is frozen into the ion fluid motion and the dy-
 125 namics is correctly described by ideal MHD. During this phase the system spontaneously
 126 starts to distort and shrink the initial current sheet, eventually reaching a characteristic width
 127 comparable with the ion inertial length d_i . As a result, where the magnetic configuration is
 128 favourable, Hall-reconnection sets in on a fast time scale [Birn *et al.*, 2001; Faganello *et al.*,
 129 2008c, 2012a]. Admittedly, our model neglects the kinetic dynamics at scales smaller than
 130 d_i , as well as possible anisotropy effects [see, e.g., Cerri *et al.*, 2013; De Camillis *et al.*,

131 2016, and references therein]. Nevertheless, when implemented for reproducing a large por-
 132 tion of the boundary our model can realistically evaluate reconnection-induced plasma ex-
 133 changes at the magnetopause [see *Henri et al., 2013*]. Indeed we are not interested in the
 134 kinetic details of the reconnecting structures, such as ion and electrons exhausts, particle ac-
 135 celeration or particle streaming along newly reconnected lines but on the modification of the
 136 global magnetic topology during the KH evolution. For this purpose a Hall-MHD descrip-
 137 tion is sufficient since it is able to catch the correct reconnection rate and thus to describe
 138 correctly the modifications of the global topology during the time-evolving configuration
 139 created by the KHI.

140 The model equations are integrated numerically using a 4th order Runge-Kutta scheme.
 141 Spatial derivatives are calculated using 6th order explicit finite differences along the peri-
 142 odic y and z directions, while a 6th order implicit compact scheme with spectral-like reso-
 143 lution [*Lele, 1992*] is adopted along the inhomogeneous x -direction. Very short wavelength
 144 fluctuations are dissipated using high order spectral filters acting only on the high- k part of
 145 the spectrum [*Lele, 1992*].

146 Special care is devoted to the boundaries along the inhomogeneous x -direction where
 147 we adopt transparent conditions for any MHD alfvénic or sonic perturbation generated inside
 148 the numerical domain. This method is based on projected characteristics of the ideal-MHD
 149 set of equations allowing one to control the in/out flux at the boundaries [*Hedstrom, 1979*;
 150 *Thompson, 1990*; *Landi et al., 2005*; *Faganello et al., 2009*]. In order to deal with the non-
 151 ideal MHD terms of our set of equations, such as the Hall and the diamagnetic terms in the
 152 Ohm’s equation, we gradually smooth them out in a buffer regions close to the boundaries.
 153 We set the boundaries far enough from the central region where small-scale structures de-
 154 velop during the dynamics and where non-ideal effects are thus important. Thus, we do not
 155 observe any spurious reflection neither at the boundaries nor in the buffer regions.

156 Simulations are initialized starting from a 2D ideal MHD equilibrium taken as uni-
 157 form along the flow direction (y -coordinate). The x and z axis are set perpendicular to the
 158 unperturbed magnetopause and along the northward direction, respectively. In this configura-
 159 tion all equilibrium quantities are functions of ψ only, where $\psi = \psi(x, z)$ is a magnetic flux
 160 function satisfying the Grad-Shafranov equations [*Andreussi et al., 2012*; *Faganello et al.,*
 161 *2012a,b*].

$$\Delta\psi = \frac{d}{d\psi}\Pi \quad ; \quad \Pi = P_{0,i} + P_{0,e} + B_{0,y}^2/2 \quad (7)$$

162 Setting $\Pi = cst$ a simple solution is given by

$$\psi_0(x, z) = \frac{1 + \delta}{2}x + \frac{1 - \delta}{2} \frac{L_z}{2\pi} \sinh \frac{2\pi x}{L_z} \cos \frac{2\pi z}{L_z} \quad (8)$$

163 while the other equilibrium quantities are set as

$$n_0 = 1 \quad (9)$$

164

$$\mathbf{u}_0(x, z) = \frac{u_\star}{2} \tanh \frac{\psi_0(x, z)}{\ell_\star} \mathbf{e}_y \quad (10)$$

165

$$\mathbf{B}_0(x, z) = \nabla \times \psi_0(x, z) \mathbf{e}_y + \frac{\tan(\varphi)}{2} \left[1 + \tanh \frac{\psi_0(x, z)}{\ell_\star} \right] \mathbf{e}_y \quad (11)$$

166

167

168

169

170

171

172

where φ is the shear angle between the magnetospheric field and the IMF. The first term in Eq. (11) corresponds to the northward magnetospheric field ($x < 0$) and the dominant northward component of the IMF ($x > 0$). The second term adds a flow aligned component to the IMF, taking into account possible different configurations that are observed during periods of northward IMF. The equilibrium thermal pressure $P_{0,i} + P_{0,e}$ is the dominant term in Π and varies from the magnetosphere to the magnetosheath in order to compensate for the increasing of $B_{0,y}^2/2$. A sketch of this equilibrium configuration is given in Fig. 1.

173

174

175

176

177

178

179

180

181

182

183

184

185

186

187

In our simulations we set $L_z = 120\pi$ and $\delta = 1/3$ so that the northward component of the magnetic field is nearly straight inside within the interval $-L_x/2 < x < L_x/2$, with $L_x = 90$. Setting $\ell_\star = 3 \ll L_x$ we obtain an equilibrium configuration that varies mainly along the x -direction and a velocity shear layer vorticity at $x = 0$ that is three times larger at $z = 0$ than at $z = \pm L_z/2$. As a consequence the KH instability, whose maximal growth rate is a fraction of the velocity shear layer vorticity [Drazin and Reid, 1981], develops far faster in the equatorial region than at higher latitudes. This initial 2D configuration permits to mimic the preferential equatorial development of the KH instability at the flank magnetopause, under northward IMF. In the case of the Earth's magnetosphere, however, stabilization at higher latitudes is expected and observed owing to magnetosheath flow and magnetic field draping properties, so that magnetic and flow fields become more aligned and thus less prone to KH development [Chandrasekhar, 1961]. The box dimension along the flow is $L_y = 2\lambda_{FGM,z=0} = 30\pi$, where $\lambda_{FGM,z=0}$ is the expected wavelength of the fastest growing mode as given by a simplified 2D stability analysis at the equatorial plane. The number of grid points along each direction is given by $n_x = 900$, $n_y = 512$, $n_z = 512$.

188

189

190

The sonic and alfvénic Mach number are defined as $M_s = u_\star/c_s$ and $M_A = u_\star/v_{A,z}$, where c_s and $v_{A,z}$ are calculated at the centre of the numerical box. Their values, together with the other parameters, are listed in table 1. Finally, we take $P_i = P_e$ and $\eta = 0.001$.

run	M_A	M_s	$\tan(\varphi)$	description
"A"	1.0	$\sqrt{3/5}$	0.3	weak magnetic shear
"B"	2.0	$\sqrt{12/5}$	1.0	strong mag. shear & high velocity

191 **Table 1.** Summary of the relevant parameters characterizing the different simulations.

192 In order to follow the system evolution, to individuate the plasma structures forming
 193 during the dynamics and to follow the field line connectivity, we define a passive tracer ζ
 194 advected by the fluid so as to mark the two different plasmas during the evolution. At the
 195 beginning of the simulation the passive tracer is set as

$$\zeta(x, z) = 0.6 + 0.4 \tanh \left[\frac{\psi_0(x, z)}{\ell_\star} \right] \quad (12)$$

196 where $\zeta < 0.6$ corresponds to the magnetospheric plasma and $\zeta > 0.6$ to the solar wind one
 197 while $\zeta \simeq 0.6$ determines the position of the magnetopause. The passive tracer ζ is constant
 198 along each magnetic field line and evolves as the field lines would do within ideal MHD. In
 199 this way ζ allows us to identify the reconnected lines linking the magnetospheric and solar
 200 wind plasma as those along which a variation of ζ is measured.

201 **3 Large-scale dynamics of KH vortices**

202 **3.1 Overview of the dynamics**

203 As expected, from the initial white noise perturbation KH waves emerge around the
 204 wavelength associated with the fastest-growing mode (FGM) as predicted by linear theory.
 205 Given the length of the numerical box, two vortices appear at the end of the linear phase (not
 206 shown here). As soon as they enter the non-linear phase the pairing process starts [*Winant*
 207 *and Browand, 1974; Miura, 1997*]. As a result the vortices eventually merge generating a
 208 single larger vortex.

209 In Fig. 2 we show the passive tracer iso-contours at $t = 460$ for run "B". For sake
 210 of clarity, the box has been doubled along the y -direction so that two pairs of coupling vor-
 211 tices appear instead of one. The semi-transparent quasi-vertical iso-surface corresponds to
 212 the magnetopause, $\zeta = 0.6$, while the dark/light blue colour correspond to the magne-
 213 to-spheric/solar wind plasma.

214 Two pairing vortices have been produced around the equatorial region, the magne-
 215 topause being wrapped inside the vortex motions. The vortex structures, as shown by the
 216 folded magnetopause, extend both into the north and into the south hemispheres and are
 217 tilted with respect to the z -axis, corresponding to a KH wavevector not aligned with the ini-
 218 tial flow. We recall that in the absence of an initial magnetic shear ($\tan \varphi = 0$), the KH vor-
 219 tex axis would be parallel to the z -axis. As expected for the chosen initial configuration, the
 220 vortices grow around the central region of the box while they are stable at high latitudes, as
 221 shown by the colour configuration in the unperturbed planes at $z = \pm L_z/2$. However, the
 222 presence of an equilibrium magnetic shear breaks the reflection symmetry with respect to
 223 the equatorial plane of our initial configuration. Indeed while \mathbf{u}_0 and $B_{0,z}$ are symmetric,
 224 $B_{0,y} \rightarrow -B_{0,y}$ for $z \rightarrow -z$: the different properties under reflection follow from the fact that
 225 the velocity is a vector while the magnetic field is an axial vector.

226 As a consequence, vortices develop differently in the northern and in the southern
 227 hemispheres, e.g. preferring the southern hemisphere for $\tan \varphi > 0$ as shown in Fig. 2 (the
 228 opposite is true for $\tan \varphi < 0$). The physical mechanism that favours one hemisphere with
 229 respect to the other is the combined action of vortex growth and field line tying at high lati-
 230 tudes as will be discussed next in Sec.3.3.

235 3.2 The tilting of unstable modes

236 The vortex tilting observed in Fig. 2 is the consequence of the presence of a magnetic
 237 shear in the equilibrium configuration. This point can be understood as follows. The most
 238 unstable modes are the ones able to minimize the magnetic tension proportional to $\mathbf{k} \cdot \mathbf{B}_0$
 239 (that counteracts the KH development) more than to maximize the driving term proportional
 240 to $\mathbf{k} \cdot \mathbf{u}_0$ (here $\mathbf{k} = 2\pi m/L_y \mathbf{e}_y + 2\pi n/L_z \mathbf{e}_z$ is the mode wavevector, m and n the mode numbers
 241 along y and z). This effect has been proven to be at work when considering 1D equilibria
 242 varying only along x [*Southwood, 1968; Walker, 1981*], but remains efficient also in our 2D
 243 equilibria with high-latitude stabilization. Indeed, the most unstable modes underlying the
 244 development of the vortex structures have a wavevector oblique with respect to the flow ve-
 245 locity and it is roughly perpendicular to the magnetic field direction (close to the velocity
 246 shear layer).

247 In order to calculate the KH growth rate analytically, we consider the limit where the
 248 flow velocity and the magnetic field are uniform in two different regions separated by a sharp

249 discontinuity at $x = 0$. In our equilibrium configuration this would correspond to the limit
 250 $\ell_\star \rightarrow 0$ and $\delta \rightarrow 1$. By assuming incompressible perturbations, the KH growth rate is given
 251 by [Chandrasekhar, 1961]

$$\gamma(k, \vartheta, M_A, \varphi) = k \cos(\vartheta) \left[\frac{M_A^2}{4} - \tan^2 \vartheta - \tan \vartheta \tan \varphi - \frac{\tan^2 \varphi}{2} \right]^{1/2} \quad (13)$$

252 where ϑ is the angle between the wavevector and the flow direction \mathbf{e}_y . This system is unsta-
 253 ble if and only if $\vartheta_- \leq \vartheta \leq \vartheta_+$, where ϑ_\pm is defined by

$$\vartheta_\pm = \arctan \left[-\frac{\tan \varphi}{2} \pm \frac{\sqrt{M_A^2 - \tan^2 \varphi}}{2} \right] \quad (14)$$

254 Once all the parameters but φ are fixed, the most unstable modes are found for

$$2\vartheta_{\max} = -\arctan \left(\frac{4 \tan \varphi}{4 - 2 \tan^2 \varphi + M_A^2} \right) \quad (15)$$

255 that is different from zero provided that $\tan \varphi \neq 0$. For small M_A and small φ we have $\vartheta_{\max} \simeq$
 256 $-\varphi/2$, so that $\mathbf{k} \cdot \mathbf{B}_0 = 0$ around the center of the velocity shear layer. For large φ the angle
 257 $\vartheta_{\max} < -\varphi/2$ because in our equilibrium configuration the magnitude of \mathbf{B}_0 is bigger in the
 258 magnetosheath than in the magnetosphere by a factor $(1 + (\tan \varphi)^2)^{1/2}$. For large M_A the
 259 stabilizing effect of the magnetic field is reduced so that the most unstable wavevector tends
 260 to be aligned with the flow ($|\vartheta_{\max}|$ decreases). Note that for $z \rightarrow -z$, the magnetic shear
 261 angle φ as well as ϑ change sign and that $\gamma(-\vartheta, -\varphi) = \gamma(\vartheta, \varphi)$.

262 Even if this model is oversimplified, it yet gives some insights about the tilt angle of
 263 oblique modes observed in the 3D compressible simulations starting from 1D equilibria
 264 with $\ell_\star \neq 0$ [Nakamura and Daughton, 2014; Adamson et al., 2016]. A moderate dis-
 265 crepancy between the predicted ϑ_{\max} and that observed in the simulations is related to the
 266 fact that the simplified model underestimates the role of the magnetic field inside the shear
 267 layer ($|x| \lesssim \ell_\star$), where the mode amplitude is larger, while overestimates its importance
 268 in the two asymptotic region ($|x| \gg \ell_\star$). This is clearly shown by our simulations where
 269 the observed angle of the most unstable modes is slightly smaller than the predicted one.
 270 The actual angle, for both run ‘‘A’’ and ‘‘B’’ is closer to $-\arctan[(\tan \varphi)/2]$ than to ϑ_{\max} : the
 271 most unstable modes tend to develop perpendicular to the magnetic field at the center of the
 272 shear layer, minimizing the stabilizing role of the magnetic tension where the velocity shear
 273 term is stronger. Note that, at the center of the shear layer ($x = 0$) the flow aligned com-
 274 ponent of the magnetic field is given by $B_{0,y} = \frac{\tan \varphi}{2}$, so that the angle between \mathbf{B}_0 and \mathbf{e}_z

275 there is not $\varphi/2$ but $\arctan[(\tan \varphi)/2]$. This is why unstable modes develop preferentially
 276 at $\vartheta_{shear} = -\arctan[(\tan \varphi)/2]$. This is shown in Fig. 3 where we plot the magnitude of
 277 the x -averaged Fourier components of u_x in the (m, n) -plane (m, n are the mode numbers
 278 as defined before) for $\tan \varphi = 0.3$ and $\tan \varphi = 1.0$. For each m number the largest am-
 279 plitude correspond to $n < 0$, i.e. to a tilted mode. The central region of the most unstable
 280 (tilted) modes observed in the simulations (gray strips) is aligned along the direction given
 281 by $\vartheta_{shear} = -\arctan[(\tan \varphi)/2]$ (dashed line), so that $\mathbf{k} \cdot \mathbf{B}_0 \simeq 0$ at the center of the
 282 shear layer. On the contrary ϑ_{max} (continuous line) slightly underestimates the tilting. For
 283 $\tan \varphi = 0.3$ we have $\vartheta_{max} \simeq 7^\circ$ and $\vartheta_{shear} \simeq 8^\circ$. For $\tan \varphi = 1.0$, $\vartheta_{max} \simeq 17^\circ$ and
 284 $\vartheta_{shear} \simeq 27^\circ$.

291 3.3 Latitudinal shift of the vortices

302 Due to the presence of the magnetic shear in the equilibrium configuration the large-
 303 scale KH vortices extend asymmetrically with respect to the equatorial plane. In particular,
 304 for $\tan \varphi > 0$, the latitude band affected by the vortex structures shifts southward, below the
 305 equatorial plane. As we will discuss later, the opposite is true for $\tan \varphi < 0$. Qualitatively
 306 this vortex shift can be explained by the differential advection of the magnetic field lines with
 307 respect to the latitude position.

308 Differential advection has been discussed in the limit $\tan \varphi = 0$, i.e. zero magnetic
 309 shear, as an important driver for the magnetic field lines dynamics [*Faganello et al.*, 2012a;
 310 *Borgogno et al.*, 2015]. Indeed, magnetic field lines embedded in the vortex structures are
 311 slowed down in the equatorial region, with respect to their unperturbed motion, since the KH
 312 phase velocity is null in our frame. On the contrary they continue to move at the unperturbed
 313 magnetosphere/solar wind velocity at high latitudes. As a consequence, magnetic field lines
 314 of different origin are stretched and arched in the opposite directions, leading to the forma-
 315 tion of intense current sheets at mid latitudes where reconnection finally occurs. When an
 316 initial magnetic shear is present, differential advection works somewhat differently. At the
 317 beginning the KH mode develops symmetrically with respect to $z = 0$ but as soon as the vor-
 318 tices start to form, differential advection becomes more and more important and, contrary to
 319 the case without magnetic shear, modifies the vortex structure in a different way above and
 320 below the equatorial plane.

321 A sketch of this mechanism is given in Fig. 4 for $\tan \varphi > 0$. We see that the initial
 322 magnetospheric and IMF lines, initially straight at $t = t_1$, are stretched by the differential
 323 advection, resulting in magnetic field lines that are increasingly bent at $t = t_2$ and $t = t_3$. As
 324 a consequence the magnetic shear is enhanced in the northern hemisphere while it is reduced
 325 in the southern one. Since the magnetic shear tends to inhibit the KH instability the location
 326 of the maximal growth rate gradually drifts southward. As a result, for $\tan \varphi > 0$, the KHI
 327 eventually develops faster in the southern hemisphere.

328 The different evolution of the magnetic shear in the two hemispheres can be quantified
 329 by looking at the peaks of electric current $J = |\mathbf{J}| = |\nabla \times \mathbf{B}|$. In Fig. 5, top frame, we plot
 330 $\max_x(\tilde{J}_{m=0}(x, z)) / \max_x(J_0(x, z))$ as a function of z for $t = 250, 300, 350$, up to the beginning
 331 of the nonlinear phase. Here J_0 is the magnitude of the equilibrium current while $J_{m=0}$ is the
 332 magnitude of the $m = 0$ mode of the total current, thus including the nonlinear modification
 333 of the equilibrium. It is clear that the $m = 0$ magnetic shear is amplified in the northern
 334 hemisphere while it lowers in the southern hemisphere, explaining the southward shift of the
 335 KH unstable region at the beginning of the nonlinear phase.

338 In the present configuration, where the vorticity $\boldsymbol{\Omega}_0$ associated with the initial sheared
 339 flow is along $+\hat{\mathbf{z}}$, the equilibrium current \mathbf{J}_0 points out the hemisphere where the magnetic
 340 shear becomes larger. In general (for $\Omega_{0,z} \lesseqgtr 0$), the symmetry properties of the mecha-
 341 nism described in Fig.4 suggest that differential advection enhances the magnetic shear in
 342 the northern hemisphere for $\boldsymbol{\Omega}_0 \cdot \mathbf{J}_0 > 0$, while the opposite is true for $\boldsymbol{\Omega}_0 \cdot \mathbf{J}_0 < 0$. As a
 343 consequence KH vortices develop more vigorously in the southern/northern hemisphere for
 344 $\boldsymbol{\Omega}_0 \cdot \mathbf{J}_0 \gtrless 0$.

345 As a reference, in Fig.5, bottom frame, we plot the normalized value of the peaks of
 346 the total current $J = |\mathbf{J}|$ at $t = 350$ as a function of z : $\max_{(x,y)}(J(x, y, z)) / \max_x(J_0(x, z))$.
 347 The maximal current increases at all latitudes due to the lateral compression of the original
 348 current sheet imposed by the KH velocity field. At the same time the current amplification
 349 is more important in the northern hemisphere as compared to the southern one because of
 350 differential advection.

351 4 Magnetic field line dynamics

352 4.1 Overview of the dynamics

353 Most field lines maintain their connections during the whole dynamics even if strongly
 354 bent and stretched by the KH vortical motion. In particular field lines on the left (right) of
 355 the magnetopause iso-surface $\zeta = 0.6$ at $t = 0$ remain on the same side. On the other hand
 356 the connections of some field lines, such as the yellow ones drawn in Fig. 6, are affected by
 357 magnetic reconnection occurring various places at the magnetopause. Now, these field lines
 358 connect two initially well separated magnetic domains, left and right of the magnetopause.
 359 This is shown in Fig. 6, where such magnetic field lines cross the $\zeta = 0.6$ iso-surface at
 360 several latitudes, from the magnetosheath (blue) to the magnetosphere (light blue), thereby
 361 connecting both sides of the magnetopause.

362 The dynamics investigated here is more complex than that discussed in *Faganello et al.*
 363 [2012a,b, 2014]; *Borgogno et al.* [2015]. It includes at the same time a pre-existing magnetic
 364 shear between the magnetosheath and the magnetospheric fields and high-latitude stabiliza-
 365 tion of the KH instability, so that reconnection can occur both as Type I or mid-latitude re-
 366 connection. The former process is driven by the pinching of the pre-existing current sheet
 367 caused by the compression in between KH vortices. Therefore it is expected to locally occur
 368 where the instability grows the most [*Chen et al.*, 1997; *Knoll and Chacón*, 2002; *Nakamura*
 369 *et al.*, 2006]. The latter is instead related to the field line differential advection and thus may
 370 be triggered at current sheets created (or modified) by this advection, far away from the main
 371 location of the KH vortices [*Faganello et al.*, 2012a,b, 2014; *Borgogno et al.*, 2015].

372 We have shown in Fig.5, bottom frame, that in the presence of a sheared magnetic field
 373 with $\tan \varphi > 0$ the combined action of differential advection and lateral compression in-
 374 creases the electric current at all latitudes but in particular in the northern hemisphere, i.e.
 375 in the hemisphere opposite to that where the vortices are most intense. On this basis we may
 376 expect that Type I reconnection would preferentially occur around the equatorial region while
 377 mid-latitude reconnection would be favoured in the northern hemisphere. In order to under-
 378 stand the development of such a complex dynamics we need to determine a quantity that can
 379 act as a proxy for where reconnection occurs.

380 **4.2 Finding reconnection: a 3D diagnostic**

381 Determining reconnection sites in a full 3D, time-dependent geometry is far from
 382 straightforward. When a pre-existing current sheet is present, the current density $|\mathbf{J}|$ and the
 383 magnetic shear already have quite “large” values, so they are not very useful when seeking
 384 for reconnecting regions. The passive tracer ζ defined above (Eq. (12)) is, instead, a conve-
 385 nient proxy for defining “reconnected” field lines since only along these lines a variation of
 386 ζ can occur, i.e, $\mathbf{B} \cdot \nabla \zeta \neq 0$. However, such a tracer cannot identify the precise location of
 387 ongoing reconnection.

388 Hence, in order to find reconnection active regions we define the following quantity:

$$\varkappa = (\partial_t + \mathbf{u} \cdot \nabla)(S_e - S_i) = (\mathbf{J} \cdot \nabla S_e)/n, \quad (16)$$

389 where Eqs. (1), (5) and (6) have been used. The idea behind this relies on the fact that in our
 390 plasma model the entropy of each species is passively advected by its respective fluid veloc-
 391 ity. A difference between the electron and ion entropy advection thus indicate regions where
 392 ions and electrons decouple which, in a Hall reconnection regime, include the reconnection
 393 regions. We thus expect that magnetic field lines passing through regions where the value of
 394 $|\varkappa|$ peaks are those undergoing reconnection. These may be either magnetic field that have
 395 not yet reconnected but that are advected by in-flows toward the center of the decoupling re-
 396 gion, or magnetic field lines that have just reconnected and are moving away following the
 397 out-flows. Indeed, we observe in simulations that, as reconnection starts to act, the recon-
 398 nected field lines highlighted using $|\varkappa|$ are those with the the largest jump of ζ , with respect
 399 to that of several hundreds of randomly generated lines. Furthermore the value of the jump
 400 of these highlighted lines increases with time, i.e. as reconnection proceeds.

408 **4.3 Latitudinal distribution of the reconnection processes**

409 In Fig.6 regions with large values of $|\varkappa|$ are shown as red surfaces for simulation “B”
 410 at $t = 460$. These active regions are all located in the upper part of the latitude band af-
 411 fected by the vortex structures, i.e. northwards with respect to the location where vortices
 412 are most intense. With respect to the vortex axis, active regions appear as large sheets in cor-
 413 respondence to the hyperbolic points of the KH velocity field (“a.” arrow) or as small scale
 414 filamentary structures aligned with the local magnetic field direction at the northernmost
 415 rippled boundary of the vortices (“b.” arrow). We recall here that the hyperbolic points are

416 located in between vortices. These sites are also called, in particular in observational papers,
417 the “trailing edges” of KH vortices

418 When thought of in the frame of past works on the topic, these reconnection regions at
419 the hyperbolic point may be associated with either Type I or mid-latitude reconnection, since
420 both can occur there even if at different latitudes. However the usual distinction between both
421 types of reconnection loses its meaning when reconnection occurs over a large range of lati-
422 tudes as observed here. We also note that the reconnecting regions appear as rather continu-
423 ous patches from the latitude where vortices are most intense to the northernmost end of the
424 region affected by the KH instability. The only distinction concerns the mechanism by which
425 reconnection is driven, i.e. how the current is enhanced. At the location where the vortices
426 are most intense the magnetic shear grows mainly due to lateral compression, while in the
427 northern regions it increases mainly because of the magnetic field bending due to differential
428 advection.

431 For determining which mechanism is at work at different latitudes, we look at the tem-
432 poral evolution of the reconnected component of the magnetic field and compare it to the
433 evolution of the velocity field generated by the KHI. The reconnected component is defined
434 as $B_{rec} = \nabla \zeta / |\nabla \zeta| \cdot \mathbf{B}$, the component normal to the ζ isosurfaces. This quantity generalizes
435 the x -component of the magnetic field created by the linear evolution of Tearing instability
436 in a 2D configuration with an equilibrium field given by $B_{0,y} = B_0 \tanh(x/l)$, described by
437 eigenfunctions of the form $B_{x,k}(x, y, t) = \tilde{B}_{x,k}(x) e^{iky} e^{\gamma_k t}$ [Faganello et al., 2012a].

440 In Fig.7 we show $|u_x|$ (left) and $|B_{rec}|$ (right) as a function of z and t for run “B”. Both
441 quantities have been averaged over x and y . $|u_x|$ gives a precise view on how and where the
442 KHI grows, in particular it develops a peak at $z = -70$, in the southern hemisphere as already
443 stressed in the previous section. $|B_{rec}|$ has the same peak at $z = -70$ but also a long “summit
444 ridge” going from the main peak to a secondary one at $z = 48$. The main peak corresponds
445 to Type I VIR, indeed it is at the same location of the maximum of u_x that compresses the
446 original sheet. The secondary peak is related to a mid-latitude reconnection mechanism: in-
447 dependently from its actual latitude, it develops far from the location where the vortices are
448 intense, at the latitude where the current is enhanced by differential advection only.

449 Type I reconnection is characterized by the fact the KH growth rate dictates the growth
450 rate of reconnection [Chen et al., 1997; Knoll and Chacón, 2002; Nakamura et al., 2006], up
451 to the early nonlinear phase. This is shown in Fig.8 where the amplitudes of the $m = 2$ mode

(the KH FGM) of u_x (blue continuous lines) and B_{rec} (blue dot-dashed lines) are drawn as a function of time for $z = -70$. The reconnected component follows that of the velocity up to $t = 400$, with a growth rate comparable with the KH one $\simeq 0.03$. On the contrary mid-latitude reconnection at $z = 48$ starts at a later time in the nonlinear phase and proceeds at a rate that is really different from that of u_x there, as shown by red lines.

Regarding the elongated reconnection regions, they are related to a small-scale rippling of the magnetopause, with a wavevector nearly perpendicular to the local magnetic field. This rippling appears at the northern edge of the region affected by the vortices and we conjecture that it is related to a secondary instability that develops during vortex pairing, namely the secondary KH instability [Cowee *et al.*, 2009; Matsumoto and Seki, 2010; Tenerani *et al.*, 2011] or Type II magnetic reconnection, i.e. reconnection related to the folding of the flow-aligned component of the magnetic field that occurs during the pairing [Faganello *et al.*, 2008b, 2009]. In the former case it would be the velocity perturbations caused by the local ideal instability to cause reconnection [Tenerani *et al.*, 2011]. In the latter it would be reconnection itself to cause the plasma motion and thus the rippling. The detailed analysis of secondary instabilities and induced reconnection is beyond the scope of this paper and will be tackled in a future work. Nevertheless contrary to what is observed in 3D simulations neglecting high-latitude stabilization [Nakamura *et al.*, 2013; Nakamura and Daughton, 2014], in our simulations secondary instabilities occurs far away from the region where the primary KH vortices are more intense.

4.4 Double reconnection processes

We define double-reconnected field lines as those lines that undergo reconnection twice at different latitudes. About half of these lines connect the magnetosheath in the equatorial region to the magnetospheric plasma at high latitudes (and viceversa). They are particularly important, as compared to once-reconnected lines that simply “open” the magnetopause (allowing for the development of an open LLBL) because they can effectively trap solar wind plasma onto closed field lines of the magnetosphere. Indeed, the flux tubes associated to these lines can be considered as new magnetospheric flux tubes with their low-latitude portion populated by solar wind particles. Also, the creation of double-reconnected flux tubes can explain the increase of the specific entropy of the cold ion population measured just inside the magnetopause [Johnson and Wing, 2009]. Indeed, a statistical survey of the low-latitude magnetosphere during northward periods shows that the cold dense popula-

484 tion of the magnetosheath leaks through the magnetopause increasing its specific entropy by
 485 a factor 5 – 20.

486 In the absence of a pre-existing shear between the IMF and the magnetospheric field
 487 double reconnection involves two locations along the same field line in the two opposite
 488 hemispheres, acting in the northern as well as in the southern hemisphere in a nearly sym-
 489 metric way. Adding a magnetic shear to the system not only breaks the symmetry but changes
 490 where and how reconnection develops. Recent MMS data show that reconnection occurs in
 491 the region where the vortices are observed and also far away from the vortex location, pos-
 492 sibly at mid-latitude [Vernisse *et al.*, 2016]. Our simulations confirm this scenario, showing
 493 that for a positive magnetic shear angle ($\tan \varphi > 0$) reconnection occurs at the same time
 494 where the vortices are most intense and in regions that are northern that this latitude (the op-
 495 posite is true for a negative magnetic shear angle, $\tan \varphi < 0$). In addition our simulations
 496 show that double-reconnected lines are generated during the late non-linear phase of the vor-
 497 tex dynamics for both $\tan \varphi = 0.3$ and $\tan \varphi = 1.0$. An example of these lines is shown in
 498 Fig.9 where lines are connected to the dark magnetosphere at high latitudes while crossing
 499 the light blue magnetosheath plasma in the central part of the box.

504 5 Conclusions

505 We have investigated the development of the Kelvin-Helmholtz instability and the in-
 506 duced reconnection processes in a geometry that models the configuration of the flanks of the
 507 Earth’s magnetosphere during periods of northward IMF by means of high-resolution Two-
 508 fluid simulations. Our initial configuration takes into account both the effect of high-latitude
 509 stabilization and of a pre-existing magnetic shear between the magnetospheric and the mag-
 510 netosheath fields. The most remarkable features of the plasma dynamics observed in this
 511 configuration are the latitude location where the KH instability grows more vigorously, the
 512 place where induced magnetic reconnection occurs and the mechanism underlying induced
 513 reconnection.

514 Concerning the first point, as soon as the IMF has a component along the flow (de-
 515 scribed by a shear angle φ in our simulations) the reflection symmetry about the equatorial
 516 plane is broken even if the density, temperature and velocity field are symmetric (the north-
 517 ward component of the magnetic field is symmetric too). In particular, we have shown that
 518 KH vortices develop asymmetrically with respect to the equatorial plane depending on the

519 sign of the pseudoscalar $\mathbf{\Omega}_0 \cdot \mathbf{J}_0$, where \mathbf{J}_0 is the equilibrium current associated to the rotation
 520 of the equilibrium magnetic field across the magnetopause and $\mathbf{\Omega}_0$ is the equilibrium vortic-
 521 ity associated to the velocity shear. When $\mathbf{\Omega}_0 \cdot \mathbf{J}_0 > 0$, KH vortices fully develop mainly in
 522 the southern hemisphere, whereas the contrary is true for $\mathbf{\Omega}_0 \cdot \mathbf{J}_0 < 0$.

523 From a physical point of view the shift of the vortices towards one hemisphere can be
 524 explained by looking at the dynamics of magnetic field lines at the beginning of the nonlinear
 525 phase. In fact, even if the linear KH growth rate is symmetric, the dynamics of field lines is
 526 not. Indeed, the magnetic field lines are frozen in the plasma fluid motion and are advected
 527 differently at high latitudes, where the magnetospheric/solar wind velocity stays unperturbed,
 528 and at low latitude where the instability develops. This differential advection causes the av-
 529 eraged magnetic field shear to increase in one hemisphere and to be reduced in the other one.
 530 Since the magnetic shear tends to inhibit the KH growth, vortices develop asymmetrically.

531 Since both $\mathbf{\Omega}_0$ and \mathbf{J}_0 change sign when passing from the magnetospheric dusk flank
 532 to the dawn flank, the hemisphere where the vortices are more intense is the same at both
 533 flanks, e.g. the southern one if the flow-aligned component of the IMF is positive. This fact
 534 can be directly inferred from the symmetry properties of the system: the dawn flank con-
 535 figuration can be obtained from the dusk one by reflecting the system with respect to the
 536 magnetopause and applying charge-conjugation. Since MHD equations are invariant under
 537 “reflection + charge-conjugation”, the large-scale KH dynamics is specular.

538 In the past, *Farrugia et al.* [1998] and *Gratton et al.* [2003] considered the impact of
 539 the clock angle of the IMF on the KH instability, i.e. the impact of a westward component
 540 of the magnetic field, perpendicular to both the northward and the flow directions. Neglect-
 541 ing the flow-aligned component of the IMF, they showed that for a positive clock angle the
 542 location of the maximum linear growth rate of the KH instability is located in the northern
 543 hemisphere at the dusk side. The opposite is true at the dawn flank so that the most unsta-
 544 ble hemispheres are different at the dawn/dusk sides. This behaviour has been obtained by
 545 looking at the configuration of the magnetic field close to the global magnetopause, taking
 546 into account the dipolar configuration of the magnetospheric field and the draping of the so-
 547 lar wind magnetic field around the magnetopause as described by a global MHD code. From
 548 a symmetry point of view this fact is not surprising since as soon as a westward component
 549 of the magnetic field is considered the global system is no more invariant under “reflection
 550 + charge-conjugation” so that the dawn and dusk large-scale dynamics are not specular (here

551 the reflection of the global system is about the plane defined by solar wind direction and the
 552 northward direction, passing through the Earth).

553 In our configuration the clock angle is not included so that the nonlinear KH activity at
 554 the flanks is specular. On the contrary when considering the clock angle but neglecting the
 555 shear angle [Farrugia *et al.*, 1998; Gratton *et al.*, 2003] the linear dynamics is anti-specular.
 556 Taking into account both the shear angle and the clock angle effect would help in clarifying
 557 satellite data analysis, in particular when KH activities measured at both flanks (at different
 558 latitudes) are compared [Hasegawa *et al.*, 2006; Nishino *et al.*, 2011; Taylor *et al.*, 2012].

559 The magnetic shear angle has a similar but opposite impact on the location where re-
 560 connection occurs, with respect to the location where the KH vortices eventually settle, since
 561 reconnection develops faster in regions where the magnetic shear is larger. The local mag-
 562 netic shear is enhanced in two different ways during the nonlinear dynamics. The first one is
 563 the pinching of the pre-existing current sheet that occurs at the hyperbolic point (in between
 564 successive vortices) of the KH velocity field, as in Type I reconnection. The second one is
 565 the modification of the pre-existing current sheet far away from the location where vortices
 566 are intense due to differential advection and field line bending. The local magnetic shear be-
 567 comes larger in the hemisphere opposite to the one where KH vortices are more developed,
 568 i.e. in the northern (southern) hemisphere for a positive (negative) $\mathbf{\Omega}_0 \cdot \mathbf{J}_0$. Both mechanisms
 569 are at work in our simulations, leading to the development of reconnection in a wide latitude
 570 range: from the location where vortices are most intense to the upper (lower) edge of the re-
 571 gion affected by KH perturbations.

572 Recent MMS observations on 8 September 2015 suggest that Type I reconnection pro-
 573 ceeds nearby vortices [Eriksson *et al.*, 2016] and that, at the same time, remote reconnection
 574 occurs probably at mid latitudes [Vernisse *et al.*, 2016]. The simulations discussed here re-
 575 produce this dynamics and further suggest that remote reconnection should be favoured
 576 in a given hemisphere depending on the initial magnetic shear (i.e., the prevailing IMF orien-
 577 tation). In particular when the flow-aligned component of the IMF is negative, as during this
 578 peculiar MMS observations, the favoured hemisphere is the southern one. This is compatible
 579 with the fact that the number of remote reconnection events observed on this day by MMS is
 580 bigger in the southern than in the northern hemisphere [Vernisse *et al.*, 2016].

581 Our simulations also show that reconnection, going on at different latitudes, is able
 582 to produce double-reconnected magnetic field lines connected to the Earth and thus to trap

583 dense magnetosheath plasma inside the magnetopause even when a significant magnetic
584 shear is present in the initial configuration. These results indicate that this double reconnect-
585 tion process associated with KH vortices is a viable mechanism to explain the formation of
586 the flank LLBL even in the presence of significant magnetic shear. Future work shall focus
587 on determining the efficiency of this mechanism as a function of the initial magnetic shear.

588 **Acknowledgments**

589 The simulations presented here have been performed at CINECA (Bologna, Italy) un-
590 der the ISCRA allocation initiative.
591

592 **References**

- 593 Adamson, E., K. Nykyri, and A. Otto (2016), The kelvin–helmholtz instability under parker-
594 spiral interplanetary magnetic field conditions at the magnetospheric flanks, *Adv. Space*
595 *Res.*, 58(2), 218–230, doi:10.1016/j.asr.2015.09.013.
- 596 Andreussi, T., P. J. Morrison, and F. Pegoraro (2012), Hamiltonian magnetohydrodynamics:
597 Helically symmetric formulation, Casimir invariants, and equilibrium variational princi-
598 ples, *Physics of Plasmas*, 19(5), 052102, doi:10.1063/1.4714761.
- 599 Birn, J., J. F. Drake, M. A. Shay, B. N. Rogers, R. E. Denton, M. Hesse, M. Kuznetsova,
600 Z. W. Ma, A. Bhattacharjee, A. Otto, and P. L. Pritchett (2001), Geospace Environmen-
601 tal Modeling (GEM) magnetic reconnection challenge, *Journal of Geophysical Research*,
602 106, 3715–3720, doi:10.1029/1999JA900449.
- 603 Borgogno, D., F. Califano, M. Faganello, and F. Pegoraro (2015), Double-reconnected mag-
604 netic structures driven by kelvin-helmholtz vortices at the earth’s magnetosphere, *Physics*
605 *of Plasmas*, 22(3), 032301, doi:10.1063/1.4913578.
- 606 Cerri, S. S., P. Henri, F. Califano, D. Del Sarto, M. Faganello, and F. Pegoraro (2013), Ex-
607 tended fluid models: Pressure tensor effects and equilibria, *Physics of Plasmas*, 20(11),
608 112112, doi:10.1063/1.4828981.
- 609 Chandrasekhar, S. (1961), *Hydrodynamic and Hydrodynamic stability*, OUP.
- 610 Chaston, C. C., M. Wilber, F. S. Mozer, M. Fujimoto, M. L. Goldstein, M. Acuna, H. Reme,
611 and A. Fazakerley (2007), Mode Conversion and Anomalous Transport in Kelvin-
612 Helmholtz Vortices and Kinetic Alfvén Waves at the Earth’s Magnetopause, *Physical Re-*
613 *view Letters*, 99(17), 175004, doi:10.1103/PhysRevLett.99.175004.

- 614 Chen, Q., A. Otto, and L. C. Lee (1997), Tearing instability, Kelvin-Helmholtz instability,
615 and magnetic reconnection, *Journal of Geophysical Research: Space Physics*, *102*, 151–
616 162, doi:10.1029/96JA03144.
- 617 Cowee, M. M., D. Winske, and S. P. Gary (2009), Two-dimensional hybrid simulations of
618 superdiffusion at the magnetopause driven by Kelvin-Helmholtz instability, *Journal of*
619 *Geophysical Research (Space Physics)*, *114*, A10209, doi:10.1029/2009JA014222.
- 620 De Camillis, S., S. S. Cerri, F. Califano, and F. Pegoraro (2016), Pressure anisotropy genera-
621 tion in a magnetized plasma configuration with a shear flow velocity, *Plasma Physics and*
622 *Controlled Fusion*, *58*(4), 045007, doi:10.1088/0741-3335/58/4/045007.
- 623 Drazin, P. G., and W. H. Reid (1981), Hydrodynamic stability, *NASA STI/Recon Technical*
624 *Report A*, 82.
- 625 Dungey, J. W. (1961), Interplanetary magnetic field and the auroral zones, *Physical Review*
626 *Letters*, *6*(2), 47.
- 627 Eriksson, S., B. Lavraud, F. D. Wilder, J. E. Stawarz, B. L. Giles, J. L. Burch, W. Baumjo-
628 hann, R. E. Ergun, P.-A. Lindqvist, W. Magnes, C. J. Pollock, C. T. Russell, Y. Saito,
629 R. J. Strangeway, R. B. Torbert, D. J. Gershman, Y. V. Khotyaintsev, J. C. Dorelli, S. J.
630 Schwartz, L. Avanov, E. Grimes, Y. Vernisse, A. P. Sturmer, T. D. Phan, G. T. Marklund,
631 T. E. Moore, W. R. Paterson, and K. A. Goodrich (2016), Magnetospheric multiscale ob-
632 servations of magnetic reconnection associated with kelvin-helmholtz waves, *Geophysical*
633 *Research Letters*, *43*, 5606–5615, doi:10.1002/2016GL068783.
- 634 Faganello, M., and F. Califano (2017), Magnetized kelvin-helmholtz instability: theory and
635 simulations in the earth’s magnetosphere context, *Journal of Plasma Physics*, *83*(6), doi:
636 10.1017/S0022377817000770.
- 637 Faganello, M., F. Califano, and F. Pegoraro (2008a), Competing mechanisms of plasma
638 transport in inhomogeneous configurations with velocity shear: The solar-wind in-
639 teraction with earth’s magnetosphere, *Physical Review Letters*, *100*(1), 015001, doi:
640 10.1103/PhysRevLett.100.015001.
- 641 Faganello, M., F. Califano, and F. Pegoraro (2008b), Numerical evidence of undriven, fast
642 reconnection in the solar-wind interaction with earth’s magnetosphere: Formation of
643 electromagnetic coherent structures, *Physical Review Letters*, *101*(10), 105001, doi:
644 10.1103/PhysRevLett.101.105001.
- 645 Faganello, M., F. Califano, and F. Pegoraro (2008c), Time window for magnetic reconnection
646 in plasma configurations with velocity shear, *Physical Review Letters*, *101*(17), 175003,

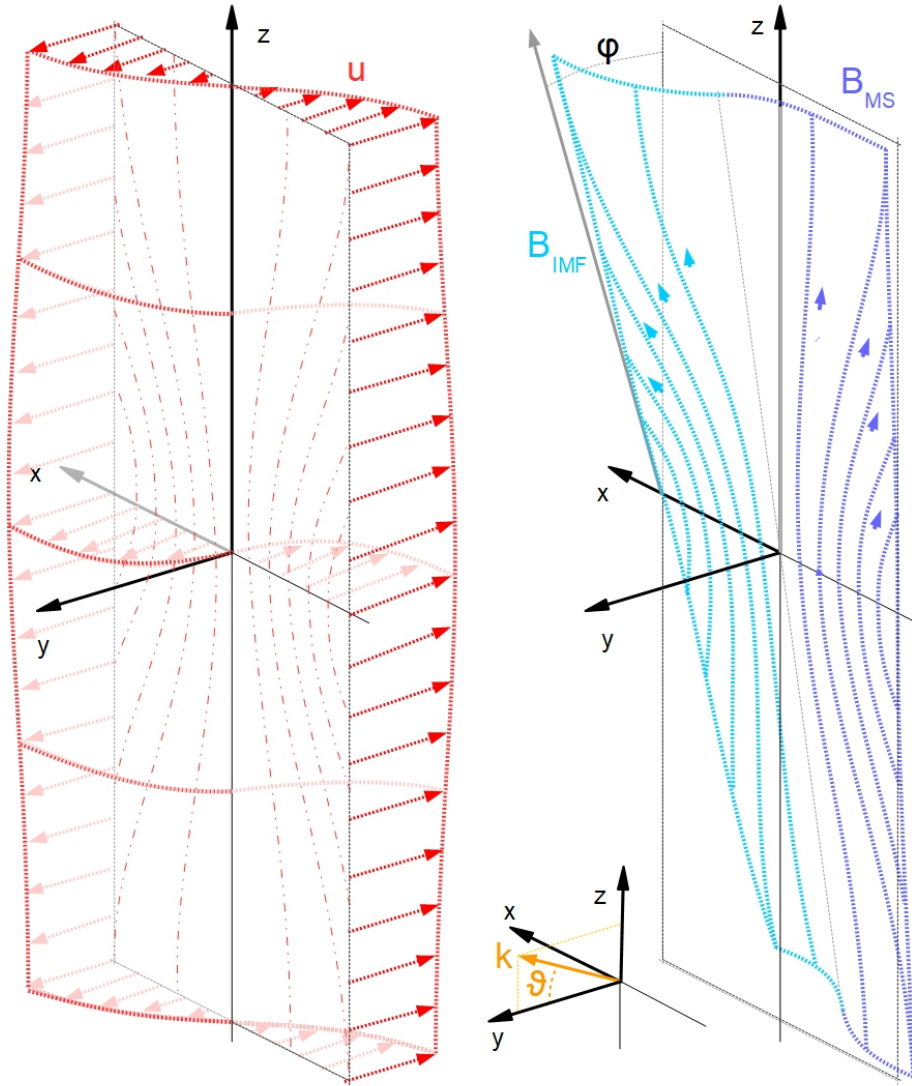
- 647 doi:10.1103/PhysRevLett.101.175003.
- 648 Faganello, M., F. Califano, and F. Pegoraro (2009), Being on time in magnetic reconnection,
649 *New Journal of Physics*, *11*(6), 063008, doi:10.1088/1367-2630/11/6/063008.
- 650 Faganello, M., F. Califano, F. Pegoraro, and T. Andreussi (2012a), Double mid-latitude
651 dynamical reconnection at the magnetopause: An efficient mechanism allowing solar
652 wind to enter the earth's magnetosphere, *EPL (Europhysics Letters)*, *100*(6), 69,001, doi:
653 10.1209/0295-5075/100/69001.
- 654 Faganello, M., F. Califano, F. Pegoraro, T. Andreussi, and S. Benkadda (2012b), Magnetic
655 reconnection and kelvin–helmholtz instabilities at the earth's magnetopause, *Plasma Phys.*
656 *Controlled Fusion*, *54*(12), 124,037, doi:10.1088/0741-3335/54/12/124037.
- 657 Faganello, M., F. Califano, F. Pegoraro, and A. Retinò (2014), Kelvin-helmholtz vortices and
658 double mid-latitude reconnection at the earth's magnetopause: Comparison between ob-
659 servations and simulations, *EPL (Europhysics Letters)*, *107*(1), 19,001, doi:10.1209/0295-
660 5075/107/19001.
- 661 Farrugia, C. J., F. T. Gratton, L. Bender, H. K. Biernat, N. V. Erkaev, J. M. Quinn, R. B.
662 Torbert, and V. Dennisenko (1998), Charts of joint Kelvin-Helmholtz and Rayleigh-
663 Taylor instabilities at the dayside magnetopause for strongly northward interplanetary
664 magnetic field, *Journal of Geophysical Research: Space Physics*, *103*, 6703–6728, doi:
665 10.1029/97JA03248.
- 666 Fuselier, S. A., B. J. Anderson, and T. G. Onsager (1995), Particle signatures of magnetic
667 topology at the magnetopause: AMPTE/CCE observations, *Journal of Geophysical Re-*
668 *search: Space Physics*, *100*, 11, doi:10.1029/94JA02811.
- 669 Gosling, J. T., M. F. Thomsen, S. J. Bame, R. C. Elphic, and C. T. Russell (1991), Ob-
670 servations of reconnection of interplanetary and lobe magnetic field lines at the high-
671 latitude magnetopause, *Journal of Geophysical Research: Space Physics*, *96*, 14, doi:
672 10.1029/91JA01139.
- 673 Gratton, F. T., G. Gnani, C. J. Farrugia, and L. Bender (2003), The stability of the pris-
674 tine magnetopause, *Planetary Space Science*, *51*, 769–783, doi:10.1016/S0032-
675 0633(03)00113-2.
- 676 Hasegawa, H., M. Fujimoto, K. Takagi, Y. Saito, T. Mukai, and H. Rème (2006),
677 Single-spacecraft detection of rolled-up Kelvin-Helmholtz vortices at the flank mag-
678 netopause, *Journal of Geophysical Research (Space Physics)*, *111*, A09203, doi:
679 10.1029/2006JA011728.

- 680 Hasegawa, H., A. Retinò, A. Vaivads, Y. Khotyaintsev, M. André, T. K. M. Nakamura, W.-
681 L. Teh, B. U. Ö. Sonnerup, S. J. Schwartz, Y. Seki, M. Fujimoto, Y. Saito, H. Rème, and
682 P. Canu (2009), Kelvin-Helmholtz waves at the Earth's magnetopause: Multiscale devel-
683 opment and associated reconnection, *Journal of Geophysical Research (Space Physics)*,
684 *114*, A12207, doi:10.1029/2009JA014042.
- 685 Hedstrom, G. W. (1979), Nonreflecting boundary conditions for nonlinear hyperbolic sys-
686 tems, *Journal of Computational Physics*, *30*, 222–237, doi:10.1016/0021-9991(79)90100-
687 1.
- 688 Henri, P., S. S. Cerri, F. Califano, F. Pegoraro, C. Rossi, M. Faganello, O. Šebek, P. M.
689 Trávníček, P. Hellinger, J. T. Frederiksen, A. Nordlund, S. Markidis, R. Keppens,
690 and G. Lapenta (2013), Nonlinear evolution of the magnetized Kelvin-Helmholtz in-
691 stability: From fluid to kinetic modeling, *Physics of Plasmas*, *20*(10), 102118, doi:
692 10.1063/1.4826214.
- 693 Johnson, J. R., and C. Z. Cheng (2001), Stochastic ion heating at the magnetopause
694 due to kinetic Alfvén waves, *Geophysical Research Letters*, *28*, 4421–4424, doi:
695 10.1029/2001GL013509.
- 696 Johnson, J. R., and S. Wing (2009), Northward interplanetary magnetic field plasma
697 sheet entropies, *Journal of Geophysical Research (Space Physics)*, *114*, A00D08, doi:
698 10.1029/2008JA014017.
- 699 Johnson, J. R., C. Z. Cheng, and P. Song (2001), Signatures of mode conversion and ki-
700 netic Alfvén waves at the magnetopause, *Geophysical Research Letters*, *28*, 227–230, doi:
701 10.1029/2000GL012048.
- 702 Knoll, D. A., and J. U. Brackbill (2002), The kelvin-helmholtz instability, differential rota-
703 tion, and three-dimensional, localized, magnetic reconnection, *Physics of Plasmas*, *9*(9),
704 3775–3782, doi:10.1063/1.1494070.
- 705 Knoll, D. A., and L. Chacón (2002), Magnetic Reconnection in the Two-Dimensional
706 Kelvin-Helmholtz Instability, *Physical Review Letters*, *88*(21), 215003, doi:
707 10.1103/PhysRevLett.88.215003.
- 708 Labelle, J., and R. A. Treumann (1988), Plasma waves at the dayside magnetopause, *Space*
709 *Science Reviews*, *47*, 175–202, doi:10.1007/BF00223240.
- 710 Landi, S., M. Velli, and G. Einaudi (2005), Alfvén Waves and Shock Wave Formation at an
711 X-Point Magnetic Field Configuration, *The Astrophysical Journal*, *624*, 392–401, doi:
712 10.1086/428822.

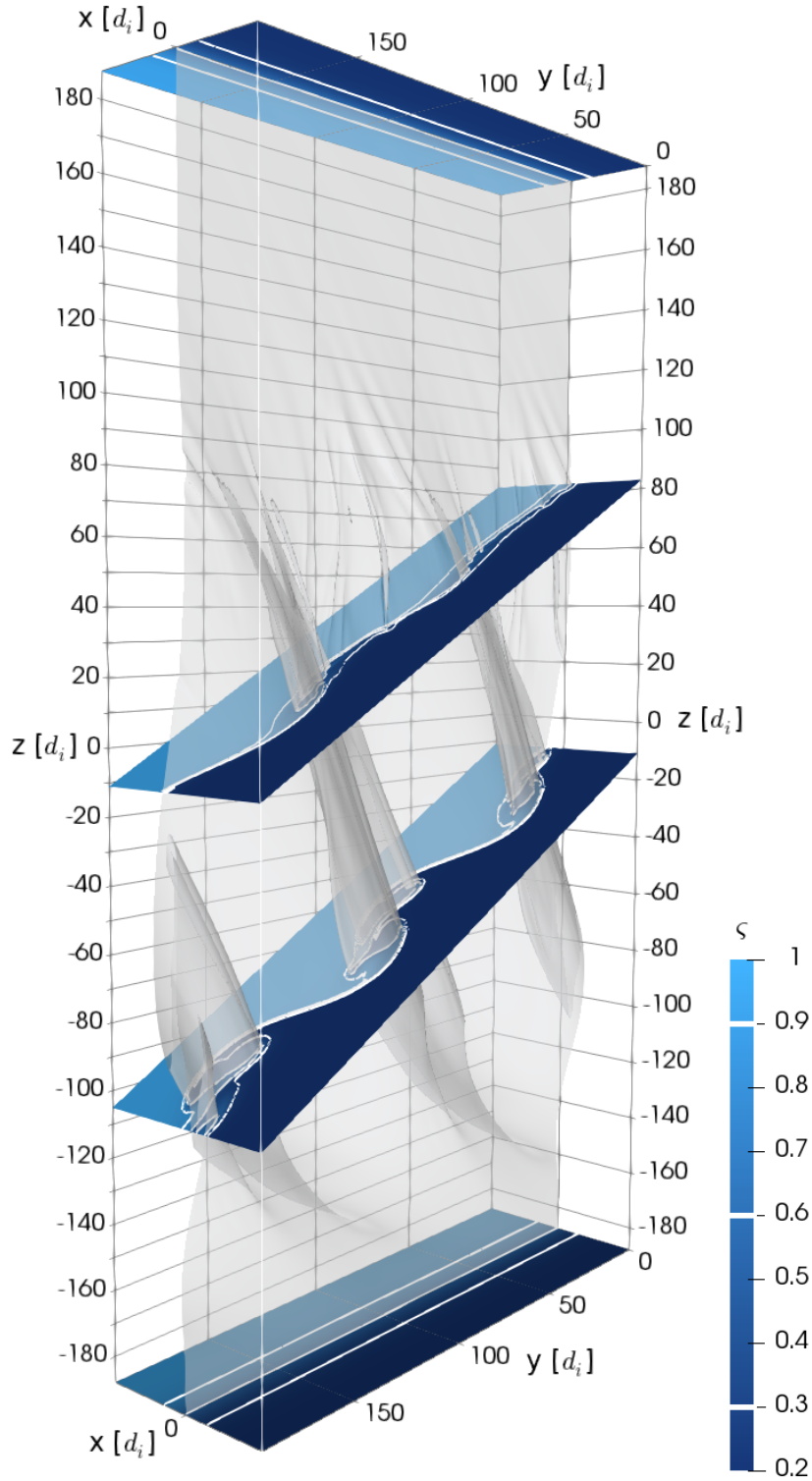
- 713 Lavraud, B., M. F. Thomsen, B. Lefebvre, S. J. Schwartz, K. Seki, T. D. Phan, Y. L. Wang,
714 A. Fazakerley, H. Rème, and A. Balogh (2006), Evidence for newly closed magnetosheath
715 field lines at the dayside magnetopause under northward IMF, *Journal of Geophysical*
716 *Research (Space Physics)*, *111*, A05211, doi:10.1029/2005JA011266.
- 717 Le, G., C. T. Russell, and J. T. Gosling (1994), Structure of the magnetopause for low Mach
718 number and strongly northward interplanetary magnetic field, *Journal of Geophysical Re-*
719 *search: Space Physics*, *99*, 23, doi:10.1029/94JA02182.
- 720 Lele, S. K. (1992), Compact finite difference schemes with spectral-like resolution, *Journal*
721 *of Computational Physics*, *103*, 16–42, doi:10.1016/0021-9991(92)90324-R.
- 722 Liu, Z. X., and Y. D. Hu (1988), Local magnetic reconnection caused by vortices in the flow
723 field, *Geophysical Research Letters*, *15*, 752–755, doi:10.1029/GL015i008p00752.
- 724 Matsumoto, Y., and M. Hoshino (2004), Onset of turbulence induced by a kelvin-helmholtz
725 vortex, *Geophysical Research Letters*, *31*, L02807, doi:10.1029/2003GL018195.
- 726 Matsumoto, Y., and K. Seki (2007), The secondary instability initiated by the three-
727 dimensional nonlinear evolution of the Kelvin-Helmholtz instability, *Journal of Geophysi-*
728 *cal Research (Space Physics)*, *112*, A06223, doi:10.1029/2006JA012114.
- 729 Matsumoto, Y., and K. Seki (2010), Formation of a broad plasma turbulent layer by forward
730 and inverse energy cascades of the Kelvin-Helmholtz instability, *Journal of Geophysical*
731 *Research (Space Physics)*, *115*, A10231, doi:10.1029/2009JA014637.
- 732 Mitchell, D. G., F. Kutchko, D. J. Williams, T. E. Eastman, and L. A. Frank (1987), An
733 extended study of the low-latitude boundary layer on the dawn and dusk flanks of the
734 magnetosphere, *Journal of Geophysical Research: Space Physics*, *92*, 7394–7404, doi:
735 10.1029/JA092iA07p07394.
- 736 Miura, A. (1997), Compressible magnetohydrodynamic Kelvin-Helmholtz instability with
737 vortex pairing in the two-dimensional transverse configuration, *Physics of Plasmas*, *4*,
738 2871–2885, doi:10.1063/1.872419.
- 739 Nakamura, T. K. M., and W. Daughton (2014), Turbulent plasma transport across the earth’s
740 low-latitude boundary layer, *Geophysical Research Letters*, *41*(24), 8704–8712, doi:
741 10.1002/2014GL061952.
- 742 Nakamura, T. K. M., D. Hayashi, M. Fujimoto, and I. Shinohara (2004), Decay of MHD-
743 Scale Kelvin-Helmholtz Vortices Mediated by Parasitic Electron Dynamics, *Physical Re-*
744 *view Letters*, *92*(14), 145001, doi:10.1103/PhysRevLett.92.145001.

- 745 Nakamura, T. K. M., M. Fujimoto, and A. Otto (2006), Magnetic reconnection induced by
746 weak kelvin-helmholtz instability and the formation of the low-latitude boundary layer,
747 *Geophysical research letters*, 33(14), L14,106.
- 748 Nakamura, T. K. M., W. Daughton, H. Karimabadi, and S. Eriksson (2013), Three-
749 dimensional dynamics of vortex-induced reconnection and comparison with THEMIS
750 observations, *Journal of Geophysical Research: Space Physics*, 118(9), 5742–5757, doi:
751 10.1002/jgra.50547.
- 752 Nishino, M. N., H. Hasegawa, M. Fujimoto, Y. Saito, T. Mukai, I. Dandouras, H. Rème,
753 A. Retinò, R. Nakamura, E. Lucek, and S. J. Schwartz (2011), A case study of Kelvin-
754 Helmholtz vortices on both flanks of the Earth's magnetotail, *Planetary Space Science*, 59,
755 502–509, doi:10.1016/j.pss.2010.03.011.
- 756 Nykyri, K., A. Otto, B. Lavraud, C. Mouikis, L. M. Kistler, A. Balogh, and H. Rème (2006),
757 Cluster observations of reconnection due to the Kelvin-Helmholtz instability at the dawn-
758 side magnetospheric flank, *Annales Geophysicae*, 24, 2619–2643, doi:10.5194/angeo-24-
759 2619-2006.
- 760 Onsager, T. G., J. D. Scudder, M. Lockwood, and C. T. Russell (2001), Reconnection at the
761 high-latitude magnetopause during northward interplanetary magnetic field condi-
762 tions, *Journal of Geophysical Research: Space Physics*, 106(A11), 25,467–25,488, doi:
763 10.1029/2000JA000444.
- 764 Otto, A., and D. H. Fairfield (2000), Kelvin-Helmholtz instability at the magnetotail bound-
765 ary: MHD simulation and comparison with Geotail observations, *Journal of Geophysical
766 Research: Space Physics*, 105, 21, doi:10.1029/1999JA000312.
- 767 Song, P., and C. T. Russell (1992), Model of the formation of the low-latitude boundary layer
768 for strongly northward interplanetary magnetic field, *Journal of Geophysical Research:
769 Space Physics*, 97, 1411–1420, doi:10.1029/91JA02377.
- 770 Sonnerup, B. U. O. (1980), Theory of the low-latitude boundary layer, *Journal of Geophysi-
771 cal Research: Space Physics*, 85, 2017–2026, doi:10.1029/JA085iA05p02017.
- 772 Southwood, D. J. (1968), The hydromagnetic stability of the magnetospheric boundary,
773 *Planetary Space Science*, 16, 587–605, doi:10.1016/0032-0633(68)90100-1.
- 774 Taylor, M. G. G. T., H. Hasegawa, B. Lavraud, T. Phan, C. P. Escoubet, M. W. Dunlop, Y. V.
775 Bogdanova, A. L. Borg, M. Volwerk, J. Berchem, O. D. Constantinescu, J. P. Eastwood,
776 A. Masson, H. Laakso, J. Soucek, A. N. Fazakerley, H. U. Frey, E. V. Panov, C. Shen, J. K.
777 Shi, D. G. Sibeck, Z. Y. Pu, J. Wang, and J. A. Wild (2012), Spatial distribution of rolled

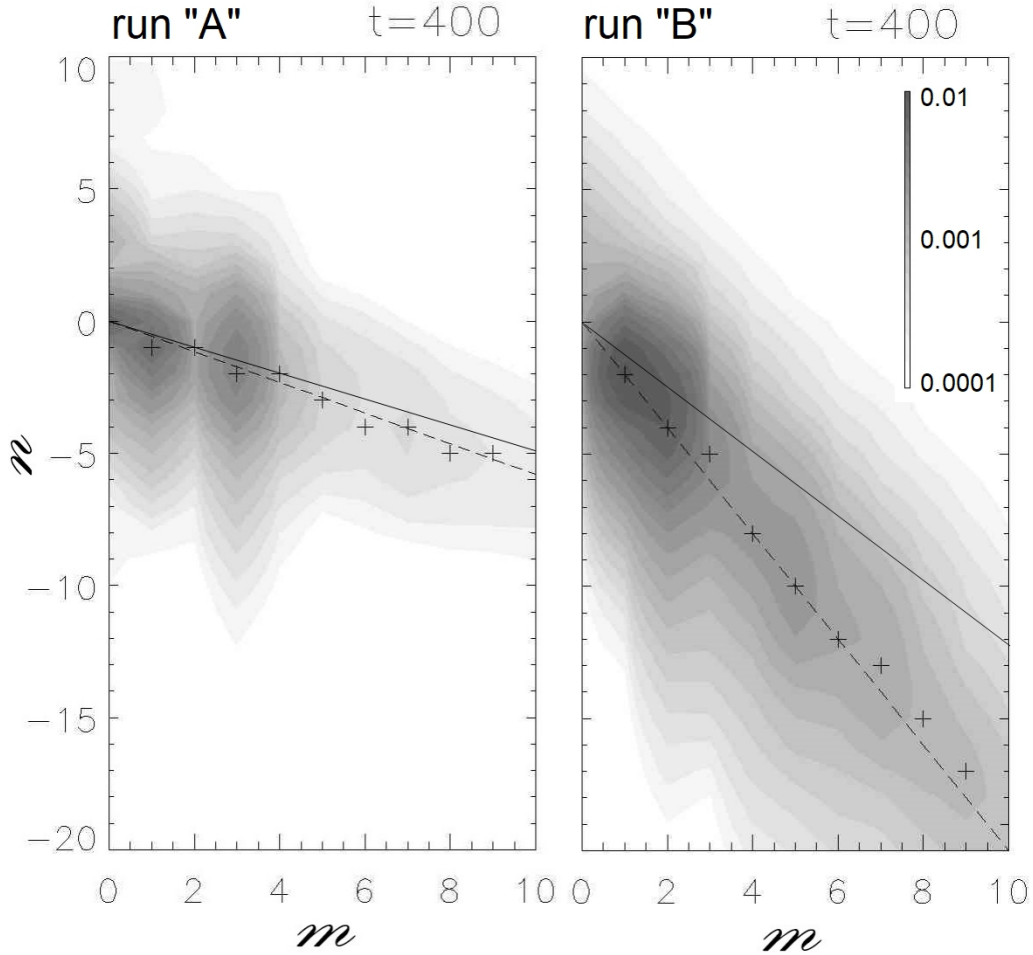
- 778 up Kelvin-Helmholtz vortices at Earth's dayside and flank magnetopause, *Annales Geo-*
779 *physicae*, 30, 1025–1035, doi:10.5194/angeo-30-1025-2012.
- 780 Tenerani, A., M. Faganello, F. Califano, and F. Pegoraro (2011), Nonlinear vortex dynamics
781 in an inhomogeneous magnetized plasma with a sheared velocity field, *Plasma Physics*
782 *and Controlled Fusion*, 53(1), 015003, doi:10.1088/0741-3335/53/1/015003.
- 783 Terasawa, T., M. Fujimoto, T. Mukai, I. Shinohara, Y. Saito, T. Yamamoto, S. Machida,
784 S. Kokubun, A. Lazarus, J. Steinberg, et al. (1997), Solar wind control of density and tem-
785 perature in the near-earth plasma sheet: Wind/geotail collaboration, *Geophysical research*
786 *letters*, 24(8), 935–938.
- 787 Thompson, K. W. (1990), Time-dependent boundary conditions for hyperbolic systems. II,
788 *Journal of Computational Physics*, 89, 439–461, doi:10.1016/0021-9991(90)90152-Q.
- 789 Vernisse, Y., B. Lavraud, S. Eriksson, D. J. Gershman, J. Dorelli, C. Pollock, B. Giles,
790 N. Aunai, L. Avanov, J. Burch, M. Chandler, V. Coffey, J. Dargent, R. E. Ergun, C. J.
791 Farrugia, V. Génot, D. B. Graham, H. Hasegawa, C. Jacquy, I. Kacem, Y. Khotyaintsev,
792 W. Li, W. Magnes, A. Marchaudon, T. Moore, W. Paterson, E. Penou, T. D. Phan,
793 A. Retino, C. T. Russell, Y. Saito, J.-A. Sauvaud, R. Torbert, F. D. Wilder, and S. Yokota
794 (2016), Signatures of complex magnetic topologies from multiple reconnection sites in-
795 duced by kelvin-helmholtz instability, *Journal of Geophysical Research: Space Physics*,
796 121(10), 9926–9939, doi:10.1002/2016JA023051.
- 797 Walker, A. D. M. (1981), The Kelvin-Helmholtz instability in the low-latitude boundary
798 layer, *Planetary Space Science*, 29, 1119–1133, doi:10.1016/0032-0633(81)90011-8.
- 799 Winant, C. D., and F. K. Browand (1974), Vortex pairing: the mechanism of turbulent
800 mixing-layer growth at moderate Reynolds number, *Journal of Fluid Mechanics*, 63, 237–
801 255, doi:10.1017/S0022112074001121.



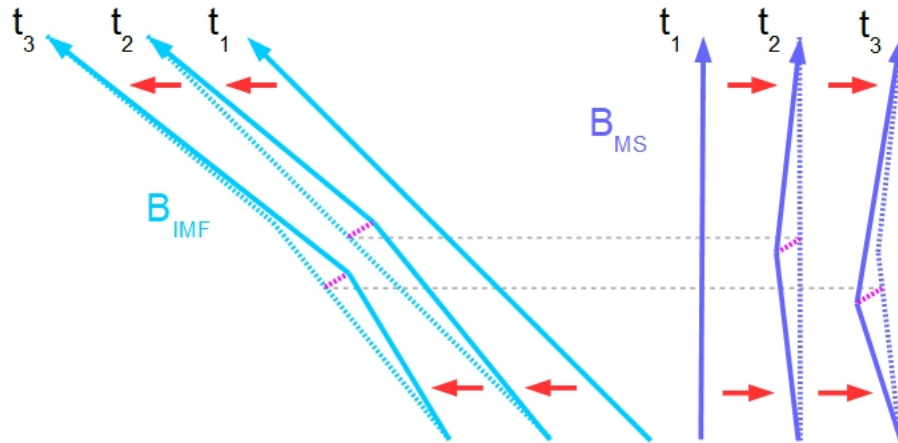
119 **Figure 1.** Schematic representation of the magnetic and velocity fields in the equilibrium configuration.
 120 φ represents the angle between the IMF and the northward direction \hat{z} . ϑ defines the angle between a given
 121 wavevector \mathbf{k} lying in the (y, z) -plane and the flow direction \hat{y} .



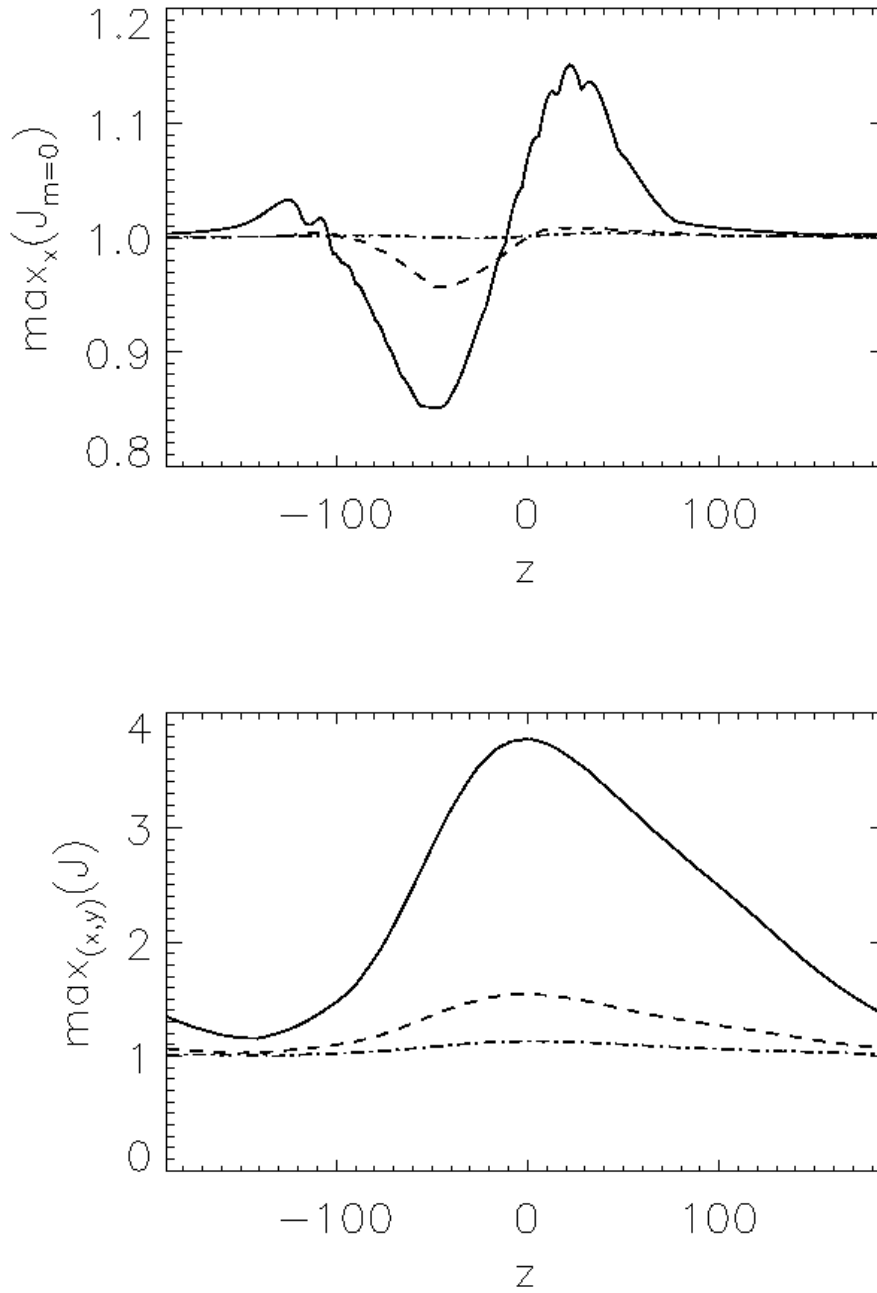
231 **Figure 2.** Visual rendering of the instability onset and development for $\tan \varphi = 1.0$ ("B" simulation) at
 232 $t = 460$. The shaded isosurface ($\zeta = 0.6$) corresponds to the magnetopause while dark/light blue colours
 233 correspond to the magnetospheric/solar wind plasmas. The white isocontours correspond to the passive tracer
 234 values $\zeta = 0.3, 0.6, 0.9$. Note that for easing the visualization the box has been doubled along the y -direction.



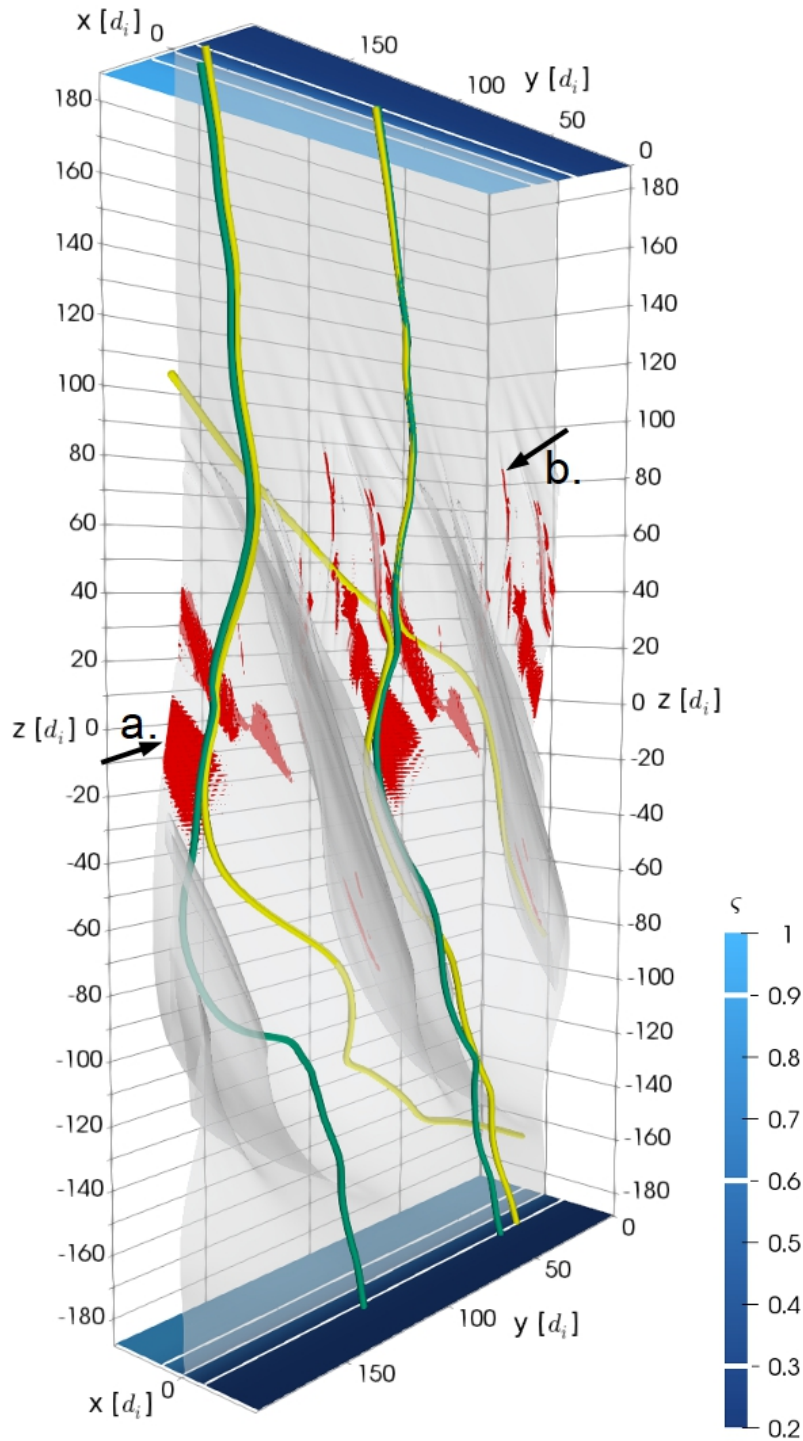
285 **Figure 3.** Shaded iso-contours of the x -averaged Fourier amplitude of u_x , normalised on the characteristic
 286 velocity u_* , taken at $t = 400$ for $\tan \vartheta = 0.3$ and $\tan \vartheta = 1.0$, left and right frames, respectively. The con-
 287 tinuous lines represent the most unstable modes given by the (n,m) couples as predicted from the analytical
 288 step-like configuration. The dashed line by $\vartheta_{shear} = -\arctan[(\tan \varphi)/2]$. For each discrete m -value, a cross
 289 indicates the location of maximal amplitude as obtained in simulations. Clearly crosses are almost aligned
 290 along the continuous line.



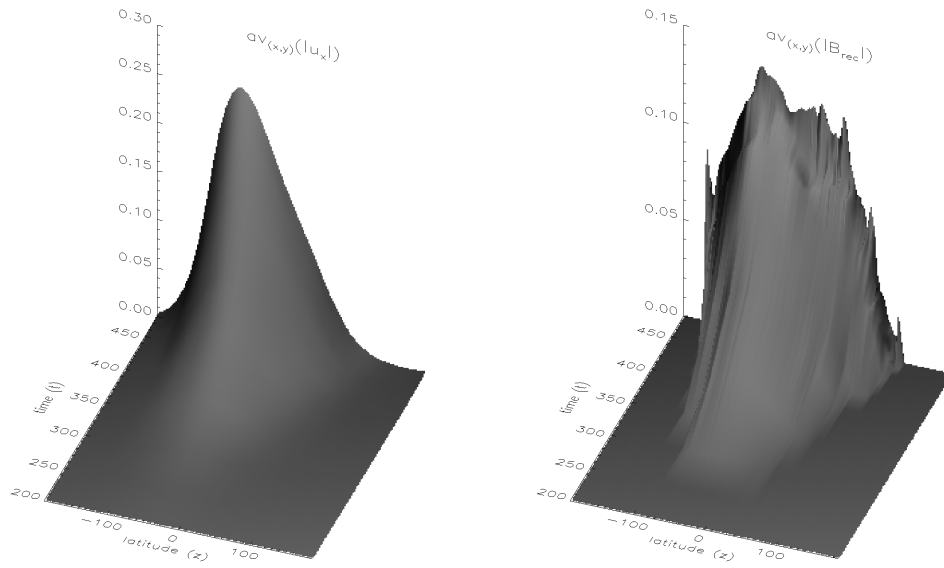
292 **Figure 4.** A sketch of the differential magnetic field line advection mechanism for $\tan \varphi > 0$. The figure
 293 shows a magnetospheric/IMF line, light blue and dark blue colours respectively, at three different times. The
 294 unperturbed field lines, denoted by t_1 , first bend close to the equators, resulting into magnetic field lines at
 295 time t_2 , due to the different advection at high/low latitudes, i.e. field lines move unperturbed in opposite di-
 296 rections at high latitudes while they are slowed down in the equatorial plane. Indeed, as the field lines are
 297 frozen into the fluid motion, they are slowed down in the equatorial plane because they are embedded in the
 298 vortex structures whose phase velocity is nearly zero. The magnetic shear is thus enhanced in the northern
 299 hemisphere and reduced in the southern one causing a southward drift of the instability. As a consequence the
 300 region where magnetic field lines are slowed down gradually shifts southward, as shown for $t = t_3$, as well as
 301 the region with smaller magnetic shear, favouring the KH development.



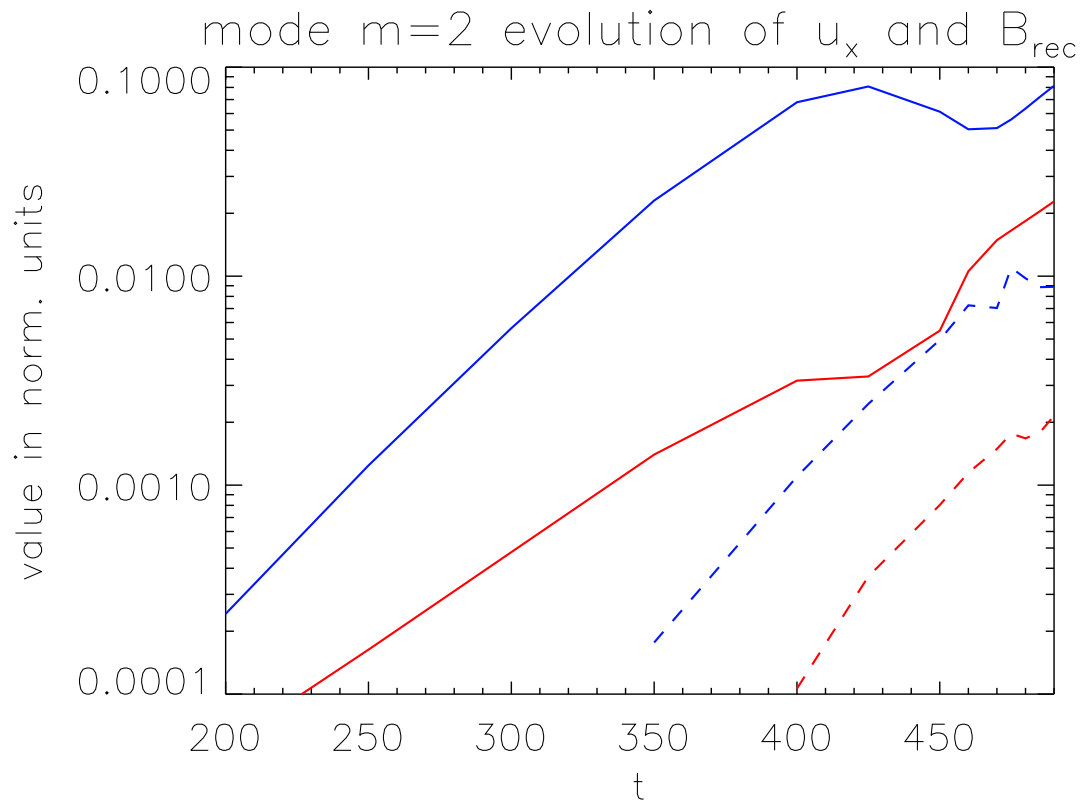
336 **Figure 5.** Top frame: $\max_x(\tilde{J}_{m=0}(x, z)) / \max_x(J_0(x, z))$ as a function of z at $t = 250, 300, 350$. Bottom
 337 frame: $\max_{(x,y)}(J(x, y, z)) / \max_x(J_0(x, z))$ at $t = 250$ (dash-dotted), $t = 300$ (dashed), $t = 350$ (continuous).



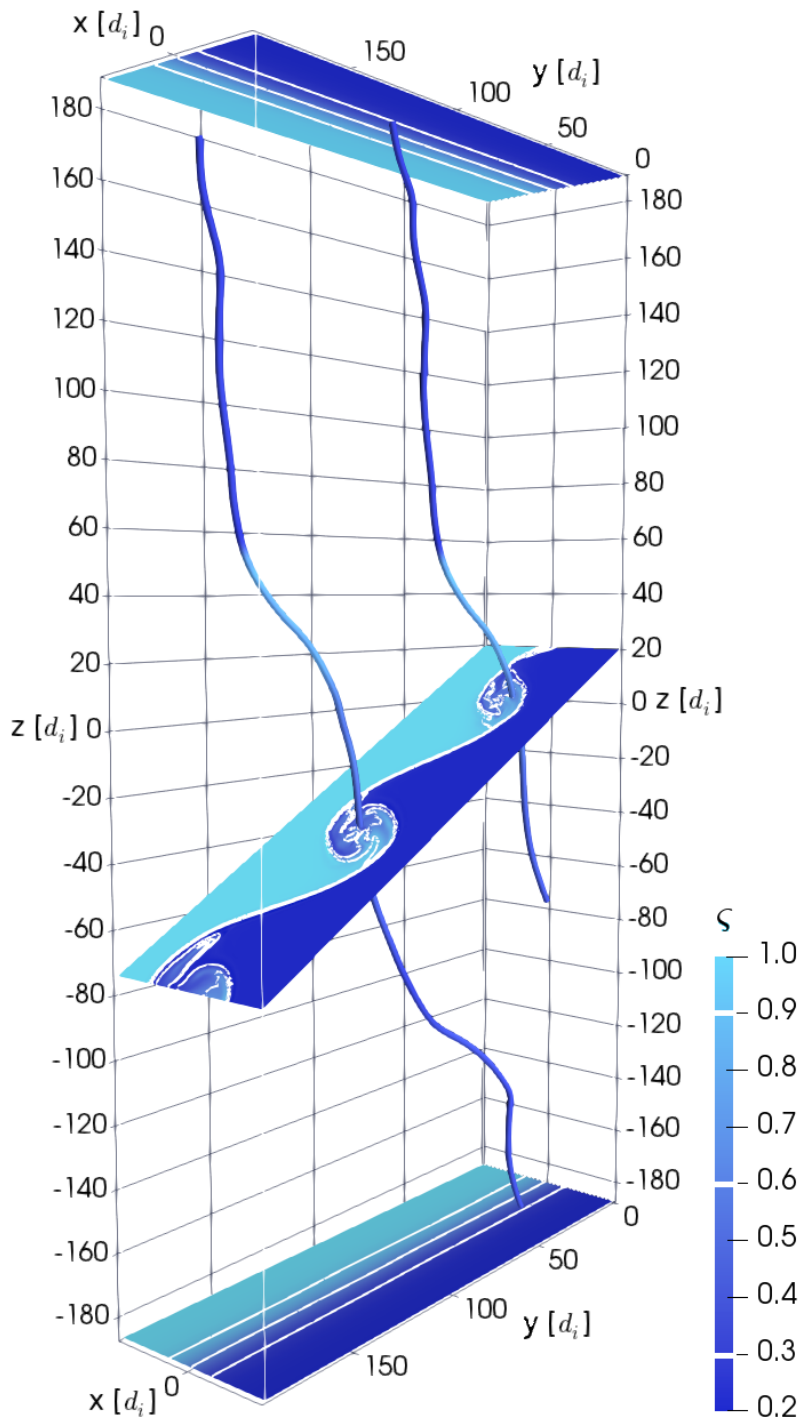
389 **Figure 6.** Shaded isosurface ($\zeta = 0.6$) corresponding to the magnetopause and dark/light blue colours
 390 corresponding to the magnetospheric/magnetosheath plasmas for $\tan \varphi = 1.0$ at $t = 460$. The white isocon-
 391 tours correspond to the passive tracer values $\zeta = 0.3, 0.6, 0.9$. The regions where reconnection takes place
 392 are enclosed in the $|z| > 0.03$ volumes, highlighted in red. The black arrows indicate planar (label “a.”) and
 393 elongated (label “b.”) reconnection sites. Some magnetic field lines representative of those crossing the active
 394 reconnecting sites have also been drawn - in yellow if reconnected, in green if not. Note that for easing the
 395 visualization the box has been doubled along the y-direction.



429 **Figure 7.** Left: $|u_x|$ averaged over x and y as a function of z and t . Right: $|B_{rec}|$ averaged over x and y as
 430 a function of z and t .



438 **Figure 8.** Time evolution of the magnitude of the $m = 2$ mode of u_x at $z = -70$ (blue continuous line) and
 439 $z = 48$ (red continuous line) and of B_{rec} at $z = -70$ (blue dot-dashed line) and $z = 48$ (red dot-dashed line).



500 **Figure 9.** Shaded isosurface ($\varsigma = 0.6$) corresponding to the magnetopause and dark/light blue colours cor-
 501 responding to the magnetospheric/magnetosheath plasmas for $\tan \varphi = 1.0$ at $t = 460$. The white isocontours
 502 correspond to the passive tracer values $\varsigma = 0.3, 0.6, 0.9$. Magnetic field lines are colored using the local value
 503 of ς . Note that for easing the visualization the box has been doubled along the y -direction.